3D PRINTING OF METAMATERIALS WITH CONDUCTIVE ELEMENTS

by

Geoffrey Glenn Tuttle

A thesis submitted to the faculty of
The University of North Carolina at Charlotte
in partial fulfillment of the requirements
for the degree of Master of Science in
Optical Science and Engineering

Charlotte

2016

Approved by:

_____

Dr. Michael Fiddy

_____

Dr. Robert Hudgins

_____

Dr. Greg Gbur

ABSTRACT

GEOFFREY GLENN TUTTLE. 3D printing of metamaterials with conductive elements. (Under the direction of DR. MICHAEL FIDDY)

To fulfill their engineered purpose, resonant metamaterials require arrays of complex three-dimensional geometries composed of non-conductive dielectrics and highly conductive materials. In order to create these geometries, 3D printers must be able to facilitate the deposition of both of these materials simultaneously. This thesis explores the conductivity requirements of two common resonant metamaterial designs, and is followed by resistance measurements on 3D printed conductive conductive doped polymer. For high conductivity, hollow channels in the shape of an extended S-split ring resonator are fabricated and injected with liquid metal. This experimental work demonstrates the feasibility of 3D printing metamaterials with conductive elements.

TABLE OF CONTENTS

LIST OF FIGURES

LIST OF TABLES

CHAPTER 1: INTRODUCTION

1.1 Metamaterials

Metamaterials are structures engineered to give a specific response to a stimulus, and are characterized by sub-wavelength geometries arranged in 3-dimensional (3D) arrays to form a bulk material. While the stimulus could be applied mechanical stress or ultrasonic sound waves[1], this project is restricting the definition to electromagnetic (EM) metamaterials.

Defining these structures as sub-wavelength does not give any absolute size constraints, but it does provide a standard to which a material must compare. Considering a well-defined unit structure of size a, a must be significantly less than the wavelength λ at which the structure is designed for interaction[2] This condition is expressed as:

$$a << \lambda = \frac{2\pi c_0}{\omega} \tag{1}$$

where c_0 is the speed of light in a vacuum and ω is the angular frequency of the EM wave.

While there is still considerable leeway in the size constraints (a desirable condition in any field of engineering), the structure must be small enough to be seen as a homogeneous material from the incident and propagating EM-waves point of view. This allows for calculation and measurement of an effective dielectric permittivity

ϵ_{eff} and effective magnetic permeability μ_{eff} of the material. In practice this is often done with feature sizes $a \approx \lambda/6$ to $\lambda/10$.

A major goal of metamaterials is to manipulate ϵ_{eff} and μ_{eff} to be simultaneously negative. This was first theorized and published by Veselago in 1968[3]. Despite this publication, the lack of an experimental concept on which to test this theory led the paper to be sidelined until fabricated structures could be realized.

In 1999, Pendry introduced a metallic wire-grid structure that could manipulate ϵ_{eff}, driving its plasma frequency ω_p into the low-GHz range[4]. This structure provided resonant interaction at previously unavailable wavelengths, leading to a tunable negative ϵ_{eff}. Pendry also introduced the split ring resonator, which interacted with the magnetic component of incident EM waves, inducing magnetic dipoles, leading to a tunable negative μ_{eff}[2].

Since these introductions, the field of metamaterials has seen steady growth with the introduction of new structures, such as variants on the split ring resonator[5], combinations of wire-grids and split rings to create simultanious negative ϵ and negative μ[6], and implementations of metamaterial theory as discrete circuit components[7].

In addition to new theoretical information and structures, the field has also seen numerous experimental verification of metamaterials. The first metamaterial with a simultaneous negative ϵ and negative μ, and therefore negative refractive index, was fabricated and verified to be operational between 10.5 and 10.8 GHz[9]. Figure 1 shows operational metamaterials since this first experimental structure. A small subset of further developments include an X-band metamaterial cloak composed of split ring resonators[10], a left-handed metamaterial operating at 100 GHz[11], a 150

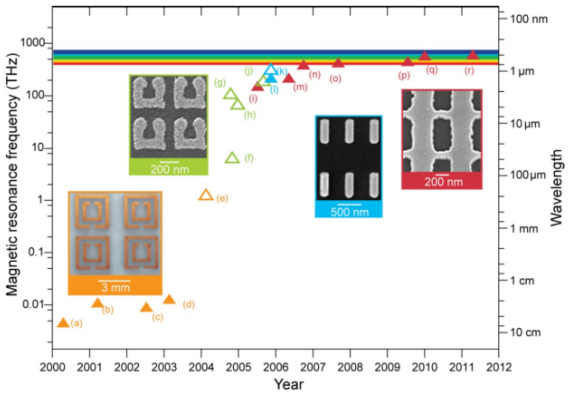

Figure 1: Metamaterial Publications by frequency: The rainbow band at the top denotes metamaterials operating at visible wavelenghts[8]

THz (near-infrared) negative index material composed of patterned gold films on a dielectric substrate[12], and a near-zero ϵ_{eff} structure in the 351 to 633 nm range[13].

This experimental work shows a steady rise in the operational frequency of metamaterial structures. This points to a future major milestone in this field, the development of a material with a refractive index of -1 over a broad band of optical frequencies. A material with this property could create the perfect lens, surpassing the diffraction limit of common imaging systems[14].

Optical frequencies correspond to wavelengths of hundreds of nanometers. With these dimensions, an operational metamaterial structure must be on the nanometer scale, as demonstrated by the equation 1.1. Although there are bulk metamaterials that operate at these wavelengths, they are heavily dependent on propagation directions, incident wave polarization, and have significant losses due to the use of metal elements[8]. Current fabrication technologies do not have the ability to demonstrate passive negative index with low-loss at this scale.

Because of these technological limitations, most metamaterial structures are devel-

oped and tested at microwave frequencies, with the intent to scale down as small-scale manufacturing abilities become available. These developments are often made at C-band and X-band frequencies (4-12 GHz), which have wavelengths between 7.5 cm and 2.5 cm. By equation 1.1, these structures must be on the order of millimeters to sub-millimeters.

1.2 3D Printing

By coincidence, the field of 3D printing (3DP) has seen a similar rapid growth after an extended period of being "under the radar." The field has its origins in the mid-1980s, when Charles Hull patented the stereolithography (SLA) method for fabricating physical objects out of an ultraviolet (UV) curing resin[15]. 3DP technology was expanded in 1990 by creating objects though inkjet deposition of liquid binder onto powdered plaster[16], and again in 1992 through fused deposition modeling (FDM), the extrusion of molten plastic into a layered, 3D structure[17].

While these technologies were expanded and new additive manufacturing methods were introduced over the next decade[18], the field as a whole began to experience exponential growth in the late 2000s. This rapid growth can be attributed to the RepRap Project. The goal of this project was to develop a 3D printer that could, eventually, fabricate all of its own parts, leading to a fully self-replicating machine. All of the software and hardware related to the RepRap Project was released under an open-source license, allowing anyone to use and modify the technology[19].

Wide access to this free information, coupled with low-cost mechanical components and printed circuit boards created numerous derivations of the RepRap Project, lead-

ing to the current ubiquity of 3DP technology. The cost of a 3D printer has dropped an order of magnitude over the past 10 years[20]. Now, for less than $1000, one of these machines can be obtained, with the ability to reliably fabricate at millimeter and sub-millimeter resolutions.

1.3 3D Printed Metamaterials

The simultaneous developments in the field of metamaterials and the field of 3DP suggests that 3D printers could be utilized in rapid prototyping of structures satisfying the geometric constraints on low-GHz range microwave-resonant metamaterials.

In fact, some progress has already been made in this field. A research group at the University of Texas at El Paso manufactured all-dielectric anisotropic metamaterials using a 3D printer[21]. Another group at the University of California in San Diego fabricated a metamaterial free-space cloak, operating at 9.9 GHz[22].

Despite the previous examples, 3DP has yet to be an integral part in resonant metamaterial fabrication. This is due to the inability of 3D printers to facilitate the deposition of both dielectric and metal materials.

1.4 Project Goals

The goal of this project is to impart, study, and improve conductivity in 3D printed materials. In addition to exploring these possibilities, this project will also incorporate highly conductive materials into 3D printed components as a post-processing step.

These goals will be achieved for the purpose of fabricating 3D printed sub wavelength sized structures already established in the field of metamaterials. These structures will be assembled into a bulk effective-media, and tested for operation in the

X- and C-band microwave regime.

CHAPTER 2: GEOMETRIC AND MATERIAL CONSTRAINTS ON METAMATERIALS

Since the publication of several sub-wavelength electromagnetic resonant structures in 1999[4][2], the field of metamaterials has rapidly expanded. By assembling bulk materials out of these engineered structures, electromagnetic phenomena unlike anything found in nature can be demonstrated.

This chapter provides a brief overview of resonant metamaterials. This is followed by an analysis of the geometric and material constraints of the the Pendry split-ring resonator (SRR) and a variant, the extended S-SRR (ES-SRR).

2.1 Permittivity, Permeability, and EM Wave Propagation

The propagation of electromagnetic waves through a material is determined by its dielectric permittivity ϵ and magnetic permeability μ.

In a vacuum, ϵ and μ are real, describing lossless propagation of the wave. All materials, however, have some form of loss. Electromagnetic wave propagation though a lossy material is determined by a complex function of ϵ and μ for homogeneous isotropic media[23]. Explicitly, these values are written as

$$\tilde{\epsilon} = \epsilon' + i\epsilon'' \tag{2}$$

$$\tilde{\mu} = \mu' + i\mu'' \tag{3}$$

where ϵ' and μ' describe the propagating component of the electric and magnetic

fields though the medium, respectively. The parameters ϵ'' and μ'' identify the loss component of the medium, causing the fields to decay exponentially as evanescent waves.

The values of ϵ and μ are directly responsible for the complex refractive index $\tilde{n}$ of a material. The relationship between these parameters is

$$\tilde{n} = \sqrt{\epsilon_r \mu_r} = \sqrt{\frac{\epsilon(\omega)\mu(\omega)}{\epsilon_0 \mu_0}}. \tag{4}$$

where ϵ_r and μ_r is the ratio of a materials permittivity and permeability to that of free space. Equation 4 highlights the frequency dependence of ϵ and μ.

Despite the wide range of permittivities and permeabilities available in natural materials, the options are not limitless. Two such examples are the lack of electromagnetic structures exhibiting negative ϵ and resonant interactions at gigahertz frequencies[4] and the lack of magnetic response in materials above these same frequencies[2].

On a fundamental level, electromagnetic waves interact with the constituent atomic particles that form the material. The values for permittivity and permeability are macrosopic averages of these individual interactions. This averaging is the basis for effective medium theory[24], and allows for simplification of a material from an assembly of individual atoms and molecules to a bulk medium, described by an effective ϵ_{eff} and μ_{eff}.

The averaging described above is an assumption on which the field of metamaterials is built. The engineered macroscopic structures seek to emulate the atomic interactions between waves and their host media. By keeping these structured "meta-

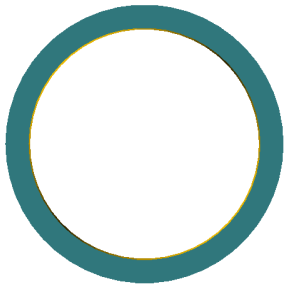

Figure 2: Single loop of conductive material.

atoms" on a sub-wavelength scale, effective medium theory allows an averaging of the interactions, generating a desired ϵ_{eff} and μ_{eff} for a bulk metamaterial.

Two such meta-atom structures are described in the following sections.

2.2 The Split Ring Resonator

The split ring resonator (SRR) was introduced as metamaterial by Pendry in 1999. This structure generates a magnetic dipole when driven by an incident magnetic field, with a resonance dependent on its geometric structure.

A thorough derivation is beyond the scope of this paper, but can be found in [2]. Borrowing heavily from this derivation, A brief introduction is as follows:

The theory of the SRR starts with a single flat loop of conducting material, as seen in figure 2. The loop is oriented perpendicular to the polarization of the incident magnetic field. This loop has a radius r and width c, where $r >> c$ and r is sub-wavelength ($r << \lambda$). These dimensional constraints allow the amplitude of the magnetic field to be averaged over the entirety of the structure, which can be treated as a single loop inductor with inductance L. As the field moves past the ring, there is a time-dependent magnetic flux though the center of the loop. As per Faraday's

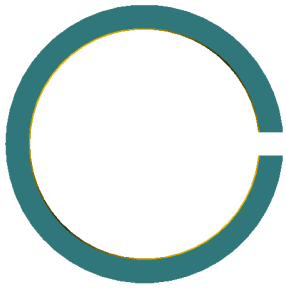

Figure 3: Single split ring

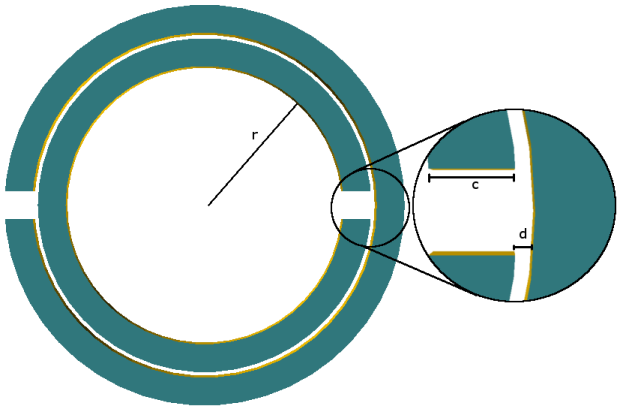

Figure 4: SRR structure

Law, the flux induces an emf in the conducting material. This emf causes a current to flow though the loop, and power is dissipated through resistance in the material.

If a small gap is introduced in the ring, as in figure 3, the induced current would be impeded, and charge would build up on opposite sides of the gap. This results in a small capacitance, and the structure could be modeled as a inductor-capacitor (LC) circuit.

Adding a second split ring at a distance d from the first completes the split ring resonator (figure 4). Since $d << r$, there is an increased capacitance C between the loops, expanding the LC-circuit model. Current flow is still impeded in the individual loops due to the gaps, but is allowed to travel between the loops because

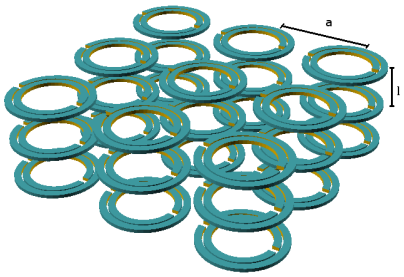

Figure 5: Split ring resonator array

of the capacitance. The current flow generates a magnetic dipole at the center of the structure, which is strongest at its resonant frequency ω_0.

The resonant frequency of an LC-circuit is dependent on the its inductance and capacitance through

$$\omega_0 = \frac{1}{\sqrt{LC}}. \tag{5}$$

Similarly, in the SRR, L and C are determined by the geometry of the individual rings (parameters shown in figure 4), with a resonant frequency derived by Pendry as

$$\omega_0 = \sqrt{\frac{3lc_0^2}{\pi ln\frac{2c}{d}r^3}}. \tag{6}$$

If the SRRs are placed in a 3D array, with horizontal separation a and vertical separation l (figure 5), multiple dipoles are created by the incident magnetic field-component of an EM-wave. These waves are augmented by the magnetic dipoles, resulting in an effective permeability μ_{eff} of the bulk metamaterial.

2.3 Resistivity Dependence of SRR

Following the derivation by Pendry, the μ_{eff} of an array of SRRs is

$$\mu_{eff} = 1 - \frac{\frac{\pi r^2}{a^2}}{1 + \frac{2l\sigma_1}{\omega r \mu_0} i - \frac{3lc_0^2}{\pi \omega^2 ln\frac{2c}{d} r^3}} \tag{7}$$

where σ_1 is the resistance per unit length of the ring, measured around the circumference[2].

Using equation 6, a SRR structure with the ring dimensions

$$a = 1.5\text{x}10^{-2}\text{m}$$

$$r = 5.0\text{x}10^{-3}\text{m}$$

$$c = 1.2\text{x}10^{-3}\text{m}$$

$$d = 1.0\text{x}10^{-4}\text{m}$$

$$l = 2.4\text{x}10^{-3}\text{m}$$

would have a resonant frequency at 3.62 GHz. This frequency depends on the geometry of the structure, while the effectiveness at manipulating μ_{eff} is dependent on the resistivity of the split-ring material.

The effect of increasing resistance is shown in figure 6. In a), a resistance of 1 kΩ/m results in a well-defined ω_0, a wide range of μ'_{eff} values, and a sharp, narrow band of high loss μ''_{eff}. As resistance increases the upper and lower peaks of μ'_{eff} are diminished, and the loss term μ''_{eff} broadens, as seen in figure 6b). Increasing the resistance further in figure 6c) and d), the propagation term μ'_{eff} no longer reaches -1, and μ''_{eff} has broadened to the point that much of the wave is attenuated in the material.

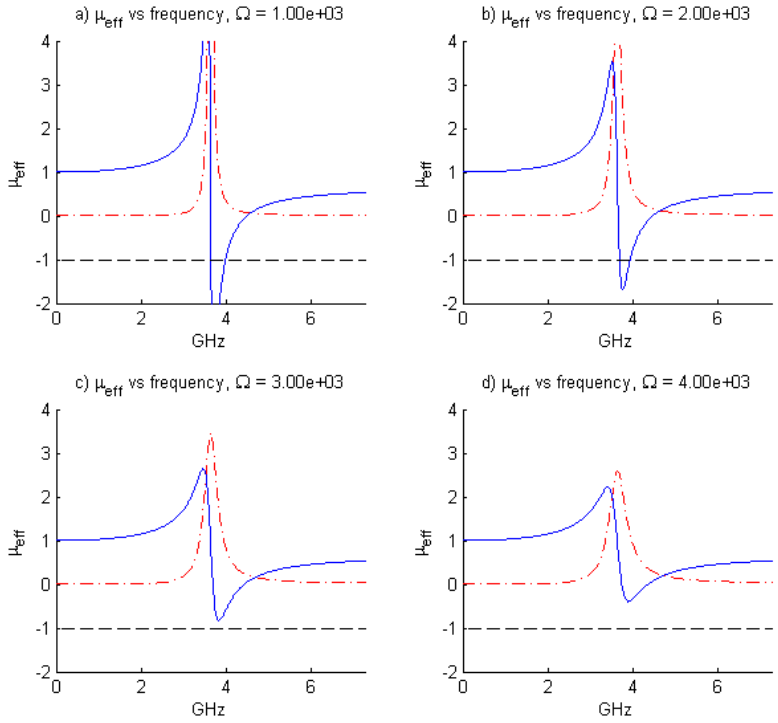

Figure 6: The resistance dependence of a SRR metamaterial. The solid blue line represents μ'_{eff}, and the dashed red line represents μ''_{eff}

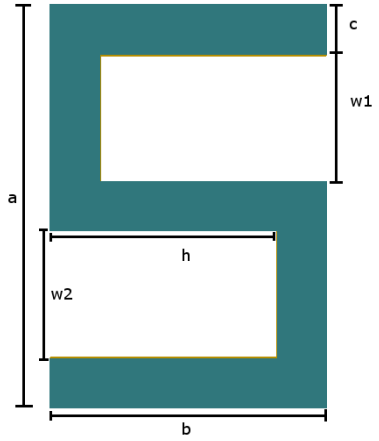

Figure 7: S-SRR dimensions

This demonstration of the resistance dependence emphasizes the need for highly conductive materials in metamaterial fabrication. The next section describes a SRR variant, the extended S-SRR (ESSRR), and presents a similar analysis of the resistivity dependence of the structure.

2.4 The Extended S-Split Ring Resonator

Developed and published by Chen in 2004, the S-split ring resonator (S-SRR) is a single structure providing both a negative ϵ_{eff} and μ_{eff}, and thus a negative refractive index[25]. This differed from previous structures utilizing a combination of components, such as a wire-grid/split ring composite metamaterial[9]. A brief overview of the magnetic response of this meta-atom, of which a thorough derivation provided by Chen can be found in [5], is as follows:

The design of the S-SRR begins with a simple S-shaped structure composed of some highly conductive material (figure 7). Similar to the SRR from section 2.2, this structure is sub-wavelength, and all electric and magnetic field amplitudes are

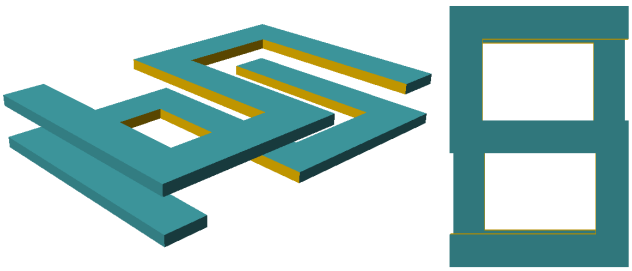

Figure 8: S-shaped element of conducting material

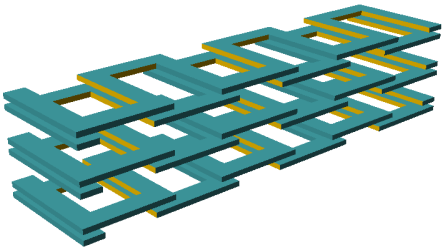

Figure 9: Extended S-SRR, separated by a distance l.

averaged over the entire structure. A distance d below the initial structure, a mirrored S-shape is placed in parallel (figure 8). As seen from a top-down view, the structure takes the form of an '8', and is a crude approximation of two loops. This provides an inductance L to the structure.

A propagating EM wave with magnetic field polarized perpendicular to the loops generates a time dependent magnetic flux though each loop. This generates an emf, inducing a current. This current is impeded in either single S-shape. Between individual structures, at the top, middle, and bottom of the 'S', there is a capacitance, allowing current to flow between mirrored elements. As with the SRR, this induces magnetic dipoles in the loops, thus creating a material with a designed magnetic response μ_{eff}.

This structure has proven to be robust and tunable. Varying the width of $w1$ and $w2$ (see figure 7) results in a structure of different sized loops. This causes a material response at multiple resonances, which allows for negative permability at multiple frequencies. The structure can also be extended and continuous (figure 9), enhancing the electric response ϵ_{eff}[5], and allowing for some unique fabrication methods to be explored in chapter 6.

2.5 Resistivity Dependence of ES-SRR

The effective permeability μ_{eff} of an extended S-split ring resonator (ES-SRR) is derived by Chen as

$$\mu_{eff} = 1 - \frac{A_1 + i\sigma l A_2 + i\sigma l A_3}{B_1 + i\sigma l B_2 + i\sigma l B_3 - \sigma^2 l^2} \tag{8}$$

where the A and B coefficients are functions of the dimensions of the structure, and σ is the conductivity in the extended-S elements[5].

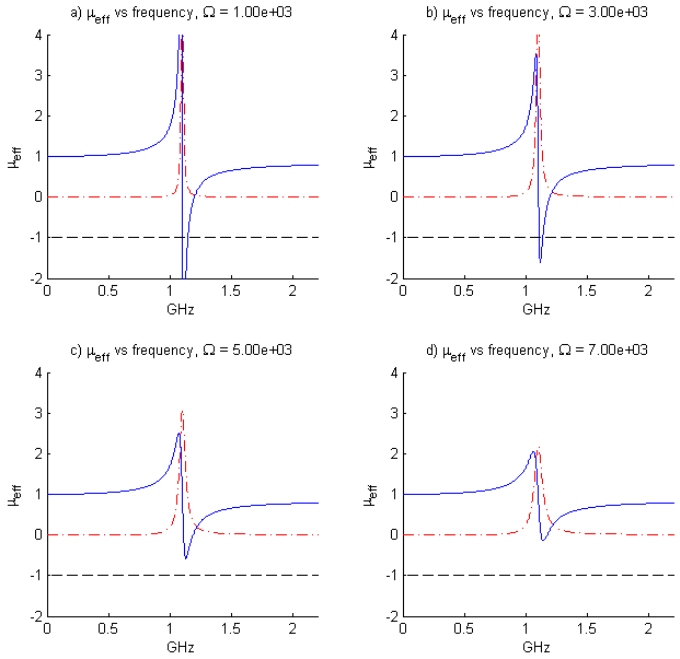

Figure 10: Relative permeability of an ES-SRR metamateral over frequency, plotted at varying resistance of material

Using the following dimensions for the ES-SRR (parameters shown on figure 7)

$$h = 3.0\text{x}10^{-3}\text{m}$$

$$w1 = 3.0\text{x}10^{-3}\text{m}$$

$$w2 = 3.0\text{x}10^{-3}\text{m}$$

$$c = 3.0\text{x}10^{-4}\text{m}$$

$$a = 11\text{x}10^{-3}\text{m}$$

$$b = 10.3\text{x}10^{-3}\text{m}$$

$$d = 2.0\text{x}10^{-3}\text{m}$$

$$l = 6.0\text{x}10^{-3}\text{m}$$

and graphing equation 8 at various material resistances, the magnetic response of the

material can be seen in figure 10, with a resonant frequency of 1.1 GHz.

Figure 10a) and b) show a wide range of relative permeabilities and a narrow imaginary μ''_{eff} This allows for operation of the material over a wide range of negative values with low-losses. As resistance increases to 5 kΩ/m in fig 10c), the loss term broadens, reducing the effectiveness of the resonance, and, in d) at 7 kΩ/m, the loss is too high to have a usable material.

2.6 Conclusions

The resistivity dependence of the structures described in this chapter highlight the need for highly conductive materials in metamaterial fabrication. For both the SRR and the ES-SRR, resistance per unit length of the resonant elements needs to be below 3 kΩ/m to achieve negative permeability with low losses.

The next chapter introduces 3D printing and commonly used 3D print material. This will serve as a foundation for the project of introducing conductive elements into 3D printed parts. The goal is to achieve low resistance material for 3D printed metamaterial components.

CHAPTER 3: 3D PRINTING TECHNOLOGY

As stated in chapter 1, 3D printing has its origins in 1986, with the patenting of the stereolithography apparatus by Charles Hull [15]. This was the first of many machines to utilize additive manufacturing methods[26]. This fabrication method differs from other "subtractive manufacturing" technologies, such as computer numerical controlled (CNC) milling, by depositing only the desired material on the build platform, and focus is placed on direct usability of the printed part[27]. This chapter describes the 3D printing methodology, and various machines that follow this process. Focus will be placed on low cost (sub-$5000 printers) and the print materials used by these devices. Print material properties will also be discussed.

3.1 3D Printing Methodology

Although there is a wide variety of additive manufacturing technologies, with distinct deposition methods and material properties[26], most follow the same operational procedure.

3.1.1 3D Model Generation

The fabrication of an object via 3D printing starts with a digital 3D model created in a computer aided design (CAD) program. This CAD file is exported in the stereolithography (STL) format, a common filetype developed by 3D Systems for use in additive manufacturing[28].

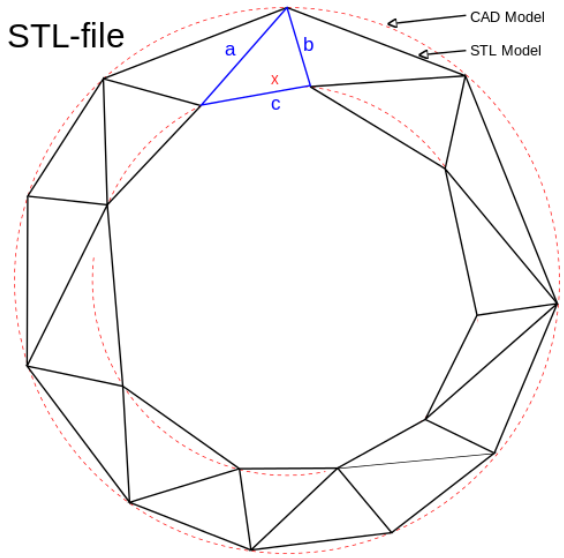

Figure 11: Comparison of CAD model to STL model. By LaurensvanLieshout (Own work) [GFDL (http://www.gnu.org/copyleft/fdl.html) or CC BY-SA 3.0 (http://creativecommons.org/licenses/by-sa/3.0)], via Wikimedia Commons

An STL file is a series of triangles defined by the location of their vertices in Cartesian coordinates and facet normals. These triangles share edges to form a mesh that takes the approximate shape of the 3D object[29] (Figure 11).

To be used in 3D printing, all features in an STL must be defined by an enclosed mesh. This avoids open surfaces that would create a structure with infinitely-thin walls, and be unreadable by the additive manufacturing machine.

3.1.2 Model to Machine Code

STL files are then imported into a slicer program. This software breaks the 3D model into a series of stacked two-dimensional layers. These layers are then translated into machine-readable code. The code is responsible for all parameters of the machine during printing, most important being the location and deposition of material to accurately fabricate the desired physical object.

The vast majority of 3D printers utilize the RS274 numerical control language, commonly known as G-code. Although this language is shared across many printers, the application of specific codes can vary from machine to machine. Even different tolerances from identical 3D printer models can render a set of G-code instructions inapplicable. This requires 3D models to be interpreted by a slicer on a per-machine basis.

The G-code controls all aspects of the printer, such as travel and material deposition rates, layer heights, and operating temperatures of heating elements. An example of a G-code movement instruction is "G1 1.1X 3.2Y 4.0Z 10F." This instructs the machine to move (G1) to Cartesian coordinate (1.1, 3.2, 4.0) while depositing material at a rate of 10 millimeters per second.

In addition to interpreting an STL model into machine code, a slicer can add support structures to parts of the STL that are offset from the build platform. The need for support is highlighted in section 3.1.3.

3.1.3 Fabrication

The actual building of a 3D printed object starts at the print bed, or build platform. Material is deposited in a layer-by-layer manner, according to the instructions from the G-code.

If the object has overhanging elements offset from the build platform, material would be deposited without a build surface or previous layer to adhere to. For parts with these features (figure 12), the slicer would have added support structures. These support structures are removed in the next step of 3DP, post-processing.

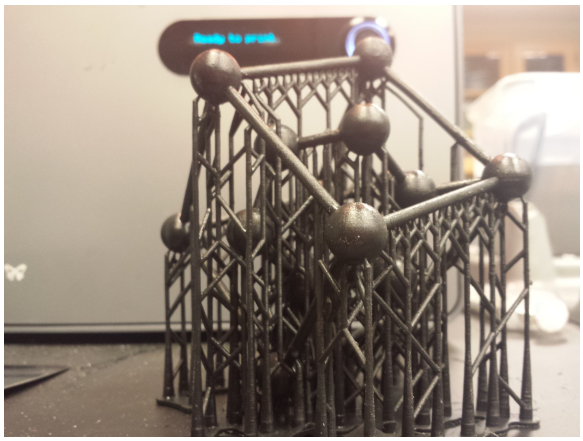

Figure 12: An example of support structures on an SLA printed silicon unit cell

3.1.4 Post-processing

After an object is printed, it is removed from the build platform. Some printing methods, such as fused deposition modeling, require little to no post-processing, and produce usable parts right from the print bed. Other methods, such as the SLA printed piece in figure 12, would require cleaning to remove uncured resin and support structures. Further processing my be required for usability, such as sanding, painting, or further curing of material in a UV oven.

3.2 Stereolithography

As stated at the beginning of Chapter 3, the first 3D printer utilzed sterolithography (SLA). The method uses an ultraviolet (UV) laser, directed by two galvanometers, to solidify liquid resin into the shape of the desired part (see figure 13). The light is projected onto the build platform, tracing a cross-section of the 3D object at this image plane. This projection cures the resin with a thickness equal to the layer height. The platform is then retracted relative to the image plane, and the UV light cures the next layer of the object[15].

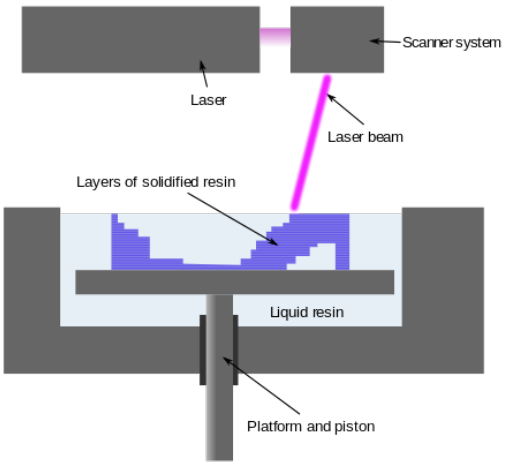

Figure 13: SLA Printing Apparatus: By User:Materialgeeza (File:Stereolithography apparatus.jpg) [CC BY-SA 3.0 (http://creativecommons.org/licenses/by-sa/3.0)], via Wikimedia Commons

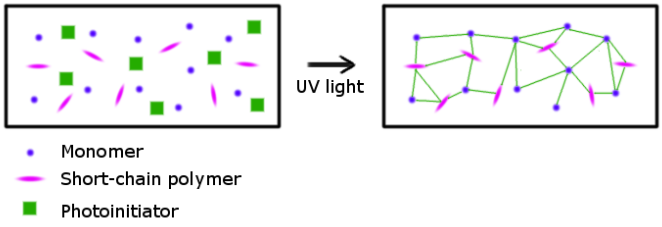

Figure 14: Photopolymerization process

After the object is created and support structures for overhanging features removed, there is a post-processing method to remove uncured resin from the part. This is accomplished by agitating the part in a cleaning bath for a short amount of time. When all resin is removed, the object is placed in a UV oven to finish curing and solidifying the part.

3.2.1 Print Material Properties

Resins for use in SLA printing are composed of a mix of monomers, short-chain polymers, and photoinitiators. In a process of photopolymerization (figure 14), the

exposure to UV light activates the photoinitiators, causing a chemical reaction that results in cross-linking between the monomers and polymers. This cross-linking is the solidification of liquid resin into a solid part[30].

Most SLA printers are closed source, and the UV resins are proprietary mixtures. This adds to the difficulty in finding standard comprehensive datasheets on the properties of objects printed with these materials.

3.2.2 Resolution

The resolution of SLA printers is determined by the UV laser spot size and the ability of the material to cross-link when activated. If the laser spot size is too small to activate enough photoinitiators, the material will not fully solidify.

The opacity of material is also a determinant of print resolution. In clear resins, the laser penetrates further into the resin tank, resulting in unwanted curing. For black resin, the laser attenuates faster, causing the material to cure in highly localized spots.

Most 3D printers state a layer resolution, which is the minimum layer height at which the printer can operate. While this is a good standard to which all 3D printers can be measured, this differs from the more useful parameter, the feature resolution. The feature resolution has significant variance depending on material type, feature orientation, and printing environment. Formlabs, the creator of the Form1+, a sub-$5000 printer used in this project, states a minimum layer resolution of 25 μm and a feature resolution of 300 μm[31].

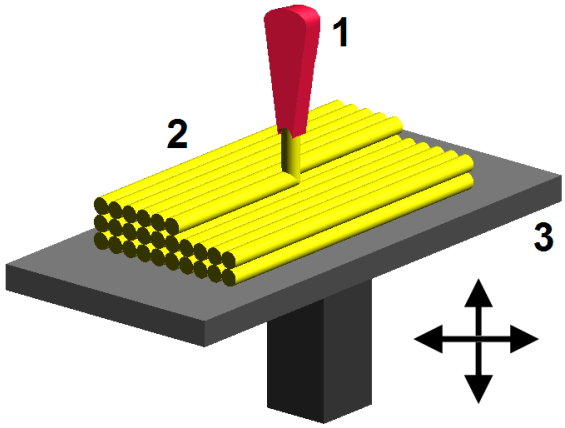

Figure 15: FDM printing apparatus with (1) hot end, (2) depositied material, and (3) mobile build platform: By Zureks (Own work) [GFDL (http://www.gnu.org/copyleft/fdl.html)], via Wikimedia Commons

3.3 Fused Deposition Modeling

Fused deposition modeling (FDM) is a method of 3D printing in which thermoplastic is fed through a heating element, mounted on a mobile gantry. This mobile heating element assembly, or print head, moves in three dimensions relative to the build platform, and deposits the print material in layered, two-dimensional slices of the desired final object (See figure 15). This method and apparatus was originally patented by S. Scott Crump, the founder of the 3D printing company Stratasys[17].

The heating element in these machines, called a hot end, is often a machined block of aluminum, with an insert for a resistive heating element, a temperature sensor, and interior threads from top to bottom. A nozzle, which determines the width of the deposited material trace, is inserted from the bottom. From the top, a PTFE plastic tube is inserted (for low friction between the thermoplastic and walls), and held in place by a heatbreak (to expand the area over which the print material is heated). Common hot ends operate from 150°C to 240°C, but all-metal hot ends, lacking the

PTFE tubing, can reach up to 300°C.

3.3.1 Print Material Properties

Virtually all FDM printers use thermoplastics as a print material. These heat-formable materials have long been used in injection molding. On a molecular level, thermoplastics are long-chain polymers with single-bond carbon backbones. The backbone structure gives the polymer chains many degrees of freedom.

Intermolecular bonds between polymer chains and their inherent high degrees of freedom produce a specific temperature common to thermoplastics, the glass transistion temperature T_g. This is the temperature at which a thermoformable plastic transitions from a hard solid to a soft, rubbery material. This occurs though the lessening of the intermolecular bonds, but not a complete breaking, that would result in a direct phase transition from solid to liquid, the melting point T_m.

Controlling the temperature T to a range $T_g < T < T_m$ keeps the material in a state of slow transition, which is desirable for deposition of thermoplastics though FDM.

3.3.2 Polymer Creep

Polymers are subject to a long-term mechanical behavior called creep. Creep is the inelastic deformation of an object that is subject to stress below its yield stress and at a temperature below its melting point[32]. It results in a change of the physical dimensions of the polymer object, the extent of which is determined by the applied pressure, compressive strength of the object, and duration over which the stress is applied.

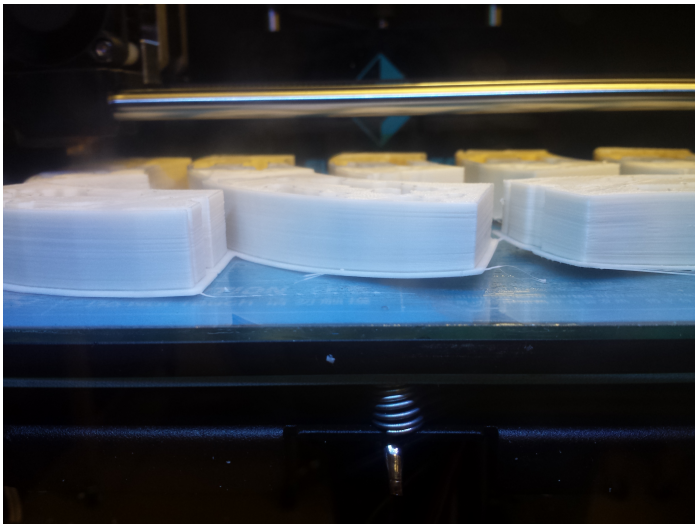

Figure 16: Example of FDM print warping

3.3.3 Print Material Availability

FDM 3D printers use spools of thermoplastic as their deposited material, often referred to as "filament." This material is sold by weight, and commonly available in 1.75 mm and 3 mm diameters.

Several thermoplastics are available in filament form for 3D printing, including acrylonitrile butadiene styrene (ABS), polylactic acid (PLA), polycarbonate (PC), and nylon being readily available.

3.3.4 Resolution

Several factors affect the feature resolution of an FDM printer. Insufficient rigidity in the printer can allow for backlash during deposition, causing placement of material at incorrect locations. Incorrect calculation of flow rates in the slicing software can cause under or over extrusion of thermoplastic during printing. The print environment can also cause a decline in feature resolution, such as a lack of adhesion on the print

bed resulting in warping (figure 16).

Ultimately, the feature resolution of an FDM printer is determined by its nozzle diameter. The diameter indicates the circular area over which material is being deposited. The FlashForge Creator Pro, an inexpensive FDM printer used in this research, comes standard with nozzle diameters of 0.4 mm. Assuming a printer with sufficient rigidity and proper calibration, low-cost FDM printers can achieve a feature resolution of 400 μm.

3.4 Conclusions

As shown in this chapter, current inexpensive 3D printers allow for the deposition of a variety of polymers at millimeter and sub-millimeter resolutions. This is sufficient to reach the geometrical fabrication tolerances for metamaterials in the low-GHz microwave regime.

The next chapter explores the possibility of adding conductive elements to print material. The resistance of printed structures with conductive particles within the thermoplastic will be tested for usability in 3D printed resonant metamaterials.

CHAPTER 4: CONDUCTIVE DOPED PRINT MATERIALS

A material is conductive if it facilitates the flow of electrons. Highly conductive solids, such as metals, have a crystal lattice structure that promotes sharing of electrons between atoms. Placing a potential across this material promotes movement of the delocalized electrons. Metals offer little resistance to this flow, and are, therefore, highly conductive[23].

Inexpensive 3D printers have yet to gain the ability to print with metal. Although there are selective laser sintering (SLS) machines that sinter metal powder into a solid object using a laser, their hazards and strict printing conditions have kept their prices high. The high temperature involved in sintering makes it incompatiable with the relatively lower temperature polymers associated with more common varieties of 3D printing.

The possibility of using conductive polymers, such as polyacetylene and polydiacetylene is attractive, but ultimatly prohibited due to their rigidity. Polyacetylene has a conjugate carbon backbone, represented in figure 17 by the alternating double and single bonds in the carbon. The carbon-carbon double bonds are overlapping

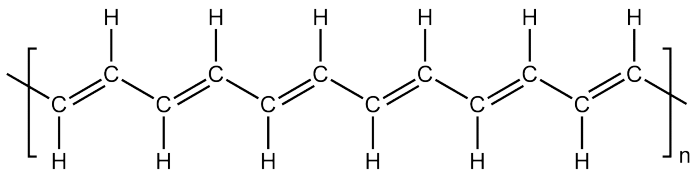

Figure 17: Structure of the conductive polymer polyacetylene

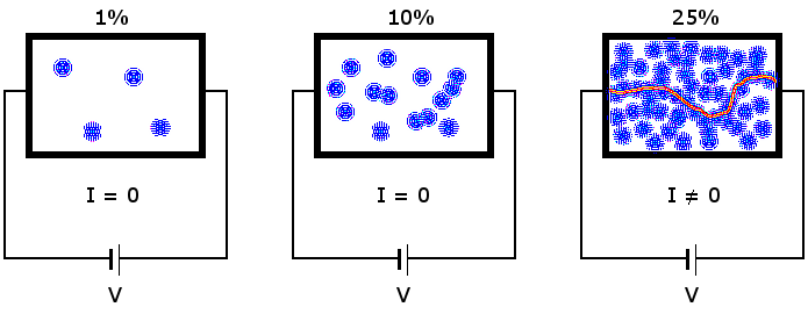

Figure 18: The percolation threshold is reached in the right image, where the volume infill of conductive particles (blue) forms a continuous path between the contacts on either side of the material.

atomic orbitals resulting in a pi bond. The alternating pi bonds along the carbon backbone result in delocalization of electrons along the polymer. This gives polyacetylene its conductivity, but also the rigidity making it not thermoformable, a necessary property for FDM 3D printing.

4.1 Extrinsically Conductive Materials

As opposed to intrinsically conductive materials, such as the previously described metals and conductive polymers, extrinsically conductive polymers derive their conductivity from conductive particles dispersed within the polymer. This project will refer to this material as a "conductive material-doped polymer composite," or a "doped polymer."

Inducing conductivity in an insulating polymer through addition of conductive particles is an application of percolation theory[33]. Conductive particles are dispersed at random in the host material. The concentration of the particles is increased until the volume infill reaches the percolation threshold. At this point, a continuous line of conductive material can be drawn from one end of the host material to the other. This provides a path for current to flow (figure 18).

While conductivity has been added to the host material, the addition of particles results in changing other parameters as well. Melting temperature, glass transistion temperature, and tensile strength of a polymer are all affected by the addition of a dopant[34]. These changes must be taken into consideration when 3D printing with a doped polymer.

4.2 Doped Polymer Printing

The recent growth of 3DP provides a new perspective on fabricating structures with these materials. Conductive doped polymers have been extruded in the form of FDM filaments, and printed for use as low-cost electronic sensors[35].

Despite the use of these materials as sensors, there has been little work in characterization of conductive material as 3D printed structures. This project seeks to measure and characterize the conductivity of 3D printed structures, for use in resonant metamaterial applications.

4.3 Research Method

4.3.1 Materials

A previous collaboration with Olivet College provided 3D prints with conductive traces. The conductive material was extruded from a spool of conductive PLA, manufactured by Proto-Plant. A spool of this material was obtained in order to fabricate objects specifically for conductivity measurements.

The manufacturer-stated resistance values for this material is 30 Ωcm measured perpendicular to the layers, and 115 Ωcm measured parallel to the layers. This accounts the anisotropic conductivity in conductive 3D prints, due to the discontinuous

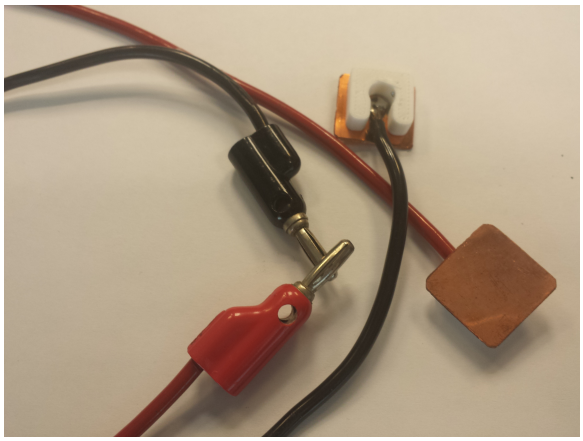

Figure 19: Custom measurement probes

nature of printing on a layer-by-layer basis.

All pieces were printed at a 0.2 mm layer height, at a hotend temperature of 205°C, and bed temperature of 60°C. The print temperature was set 10°C higher than the common 195°C for PLA to account for an increased melting point from the added dopant, and to facilitate smoother flow though the 0.4 mm nozzle.

4.3.2 Apparatus

Measurements were made with a handheld digital multimeter. For small test pieces, standard point probes were used to make contact with the conductive material surface.

To ensure full electrical contact along the surface of larger test pieces, custom probes were designed and created. Copper sheet was cut into squares measuring 2 cm x 2 cm, and soldered to a banana connector to interface with the multimeter. Plastic offsets were 3D printed and attached to the probe surface to protect the solder connection and to electrically insulate from the test environment (See figure 19).

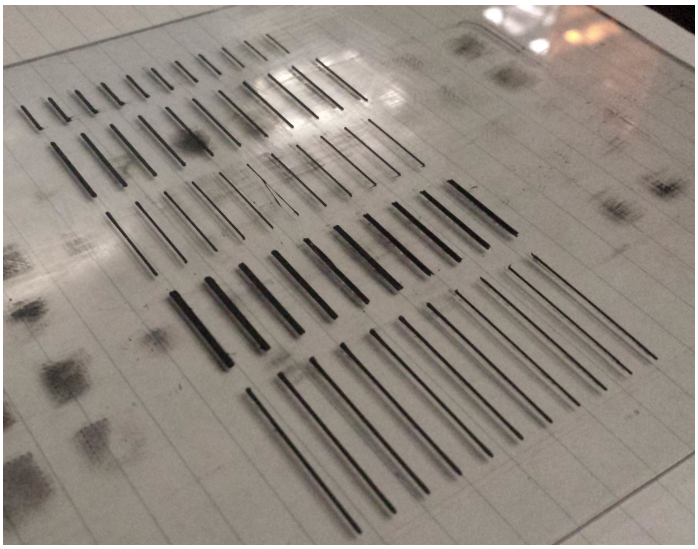

Figure 20: Conductive traces of material, printed on polycarbonate sheet

4.3.3 Measurement Techniques

Direct resistance measurements were made on the test pieces using a two terminal (2T) digital multimeter. This method was chosen as opposed to the four terminal (4T) sensing, which is used in highly conductive materials, where the contact resistance and material resistance is of the same order of magnitude. Resistance of the doped polymer was high enough that 2T sensing was deemed sufficient.

4.4 Results

4.4.1 Line Resistance

The goal of this set of measurements is to determine the resistance per unit length of thin traces of conductive doped polymer.

Using OpenSCAD as a modeling program, small rectangular prisms were generated at the dimensions found in table 1. When imported into the slicing software, these dimensions correspond to parallel printed lines of conductive material.

Table 1: CAD dimensions of printed lines

Sample	x (mm)	y (mm)	z (mm)
Single 10 mm trace	.41	10	.21
Single 20 mm trace	.41	20	.21
Single 30 mm trace	.41	30	.21
Double 20 mm trace	.81	20	.21
Triple 20 mm trace	1.21	20	.21

Table 2: Resistance measurements of printed lines

Sample	R_{ave} (kΩ)	R_{ave}/m (kΩ)/m	Std. Dev. (kΩ)
Single 10 mm trace	7.40	740	73.2
Single 20 mm trace	9.27	464	32.8
Single 30 mm trace	17.3	577	51.6
Double 20 mm trace	7.57	379	20.4
Triple 20 mm trace	4.54	227	24.1

The single width lines were to determine resistance per unit length of the material, with a cross section of 0.4 mm x 0.2 mm. These values are the nozzle width and layer height, respectively. Measurements of printed traces with a micrometer were found to be in agreement with these values. Double and triple width lines were created to determine if parallel sets of traces could be modeled as an equivalent resistance of a parallel resistor network.

Conductive lines were printed on a sheet of polycarbonate as a build platform, as seen in figure 20. Resistance measurements were conducted with point probes connected to opposite ends of the traces, separated by the length of the lines. Measurements were averaged over 15 traces each, with results seen in table 2.

4.4.2 Sheet Resistance

The goal of this set of measurements is to determine the resistance per square of the conductive polymer.

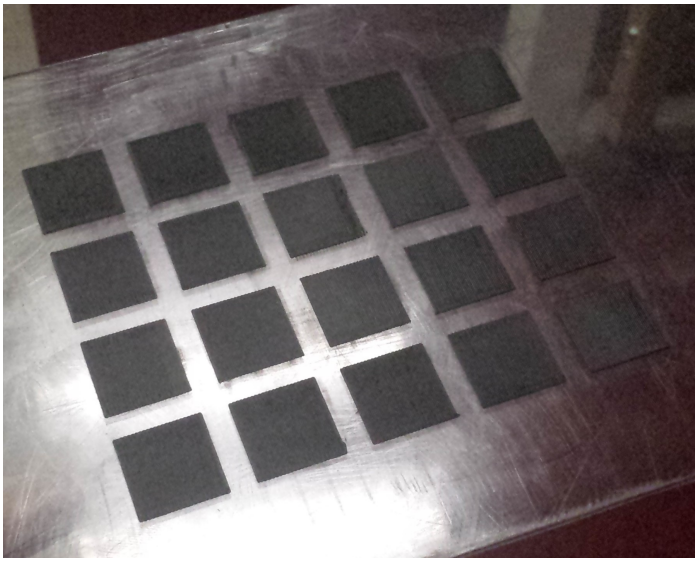

Figure 21: Conductive sheets of doped polymer, printed on polycarbonate sheet

Table 3: Resistance measurements of printed sheets

Orientation	R_{ave}/sq (kΩ/sq)	Standard Dev. (kΩ/sq)
Parallel	1.67	0.19
Perpendicular	3.16	0.36

Flattened squares were modeled in OpenSCAD with dimensions 20 mm x 20 mm x 0.2 mm. The slicing program generated G-code that would correspond to a uniform set of parallel lines.

Several sets of square conductive sheets were printed on a polycarbonate build platform (figure 21). Resistance measurements were conducted with the custom measurement probes described in section 4.3.2. The probes were used as copper bus bars and placed along the edge of each sample. Due to anisotropic resistance from the orientation of lines within the square, measurements were made from both opposite edges of the printed structure.

The resistance was averaged over 30 samples, with results seen in table 3.

Table 4: Baseline conductivity

Sample	Infill (%)	Layer Height (mm)
1	100	0.2
2	50	0.2
3	25	0.2

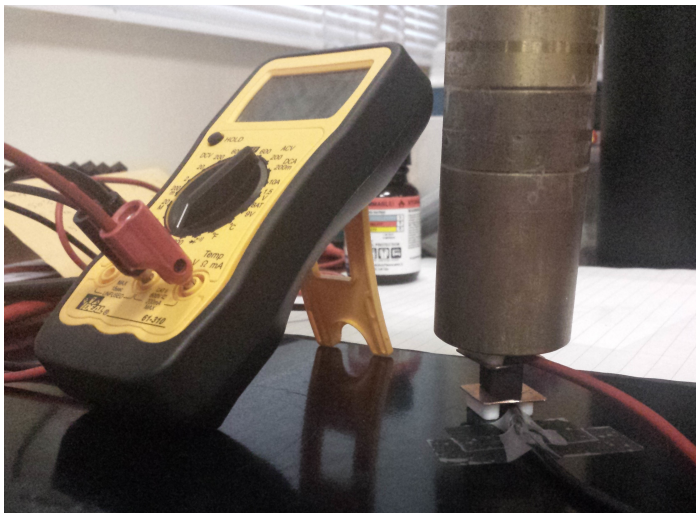

Figure 22: Conductive cube measurement apparatus

4.4.3 Bulk Resistance

The purpose of this set of measurements is to determine the bulk resistivity ρ of objects printed with conductive PLA. By printing cubes with a cross-sectional area A of 1 cm^2 and length l of 1 cm, a measured resistance R over l will be equal to the resistivity of the sample, as per equation 9.

$$\rho = R\frac{A}{l} = R\frac{1\text{cm}^2}{1\text{cm}} = R \cdot \text{cm} \tag{9}$$

To establish a bulk resistivity and standard deviation to expect from a printed part, cubes measuring $1cm^3$ were printed on a FlashForge Creator Pro FDM printer with at a 0.2 mm layer height and various infill percentages as seen in table 4.

For standardization of measurements, the surface probes (described in section 4.3.2)

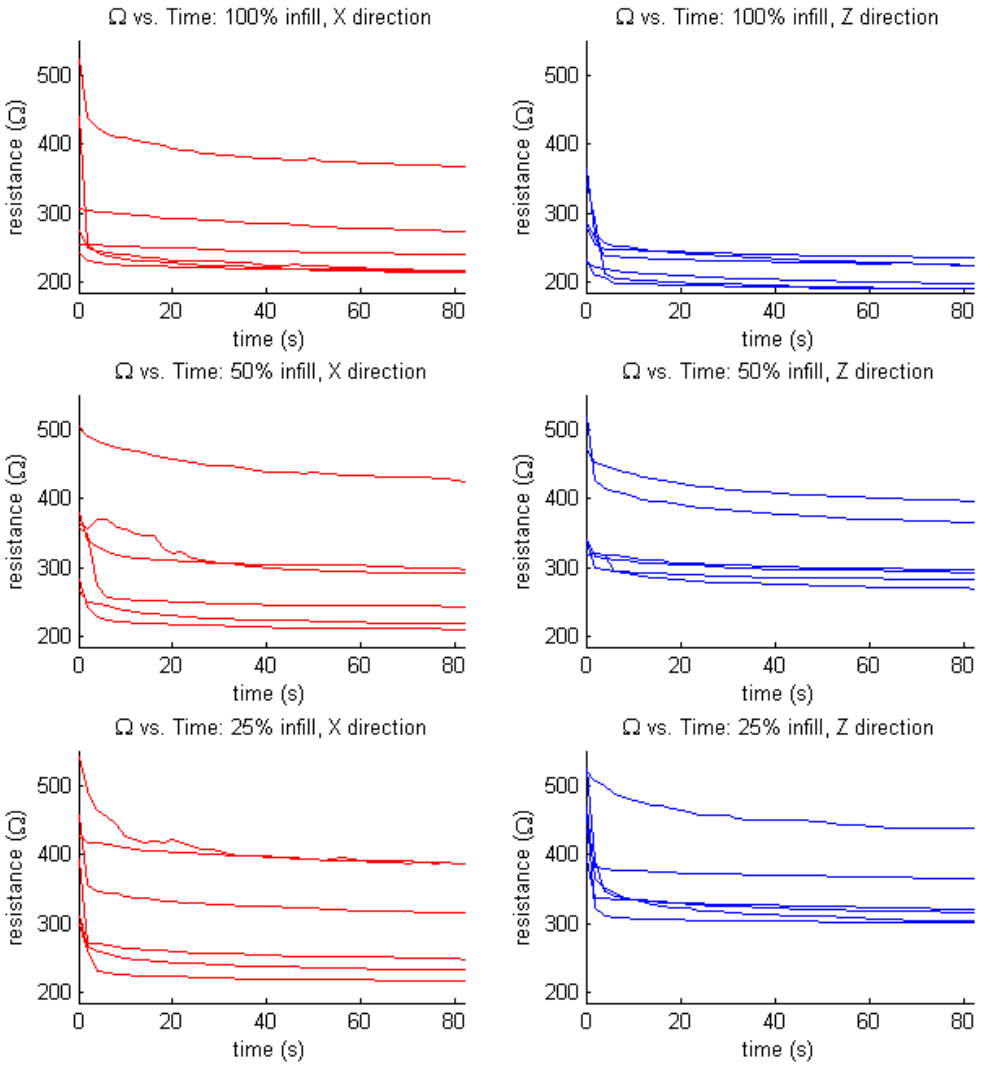

Figure 23: Resistance of various cubes under 1 kg mass

Table 5: Bulk resistivity of printed cubes

Sample	$R_{ave,x}$ (Ω)	Std. Dev. (Ω)	$R_{ave,z}$ (Ω)	Std. Dev. (Ω)	$\Omega_x < \Omega_z$
1	254	60	211	20	20%
2	281	79	317	51	67%
3	298	77	341	53	83%

were placed on the top and bottom of each of the conductive cubes. A 1.00 kg mass was placed on top of the upper probe (figure 22). This caused a time-dependent piezoresistivity to appear in the measurements. The increase in conductivity under applied pressure is a result of the polymer creep described in section 3.3.2 combined with the random dispersion of conductive particles throughout the material. Pressure forces the particles closer together, reducing the overall resistance of the material. Although the initial resistance for each cube decayed at various rates, the measurements reached a similar slope of decay after approximately 80 seconds. All final resistance values were taken at this point.

The decay in resistance in the X and Z directions can be seen in figure 23. Average resistance values, standard deviations, and the percent of cubes where $\Omega_x < \Omega_z$ is in table 5.

4.5 Discussion and Conclusions

4.5.1 Line Resistance

The overall average resistance per meter of single traces was 593 kΩ/m, with a standard deviation of 127 kΩ/m. For the purpose of resonant metamaterials, this is well above the upper limit of resistance stated in chapter 2.

Treating the printed lines as resistors, the standard deviation corresponds to a re-

sistor tolerance of 22%, which is greater than most commercially available resistors. Despite the inaccuracy, printed traces could be a viable solution to circuits requiring highly resistive components without the need for low tolerances. An example application would be a pull-up or pull-down resistor, a component used to hold a signal input to a high or low state when there is no incoming signal.

Small numbers of lines printed in parallel resulted in lower resistance, as seen in the average resistances of the double and triple traces in table 2. The equivalent resistance of N resistors R_i in parallel is given by

$$R_{parallel} = \left[\sum_{i=1}^{N} \frac{1}{R_i}\right]^{-1} \tag{10}$$

Using the average resistance per unit length, two and three of these resistors in parallel would give $R_{parallel,2} = 296$ kΩ/m and $R_{parallel,3} = 198$ kΩ/m. Both of these values fall outside of the standard deviation of the double and triple traces. A simple parallel circuit model is insufficient in describing the resistance of small numbers of parallel conductive lines.

4.5.2 Sheet Resistance

The deviation of sheet resistance measurements fell within 11% and 12% of parallel and perpendicular measurements, respectively. As with the printed line resistance, this deviation could be brought down with more uniform dispersion of conductive particles within the polymer. In its current state, this material is still to resistive for for metamaterial fabrication.

The standard deviation of the sheet resistance measurements were low, relative to

single line and bulk prints. This suggests that single layer sheets could be the most reliable method to attaining doped polymer 3D printed objects with components of known conductivity.

4.5.3 Bulk Resistance

Resistance in the x-direction had a wide variance between printed cubes of varying infill, which is represented with the lowest deviation of 24% for 100% infill. Measurements in the Z direction were more standard, with the lowest deviations from the mean falling within 9% of cubes with full (100%) infill. If a specific conductivity is needed in a 3D print of this material, the current should be propagating normal to the individual layer orientations (z-direction).

The right column of table 5 indicates how many of the test samples had a lower resistance in the x-direction than in the z-direction, which would be in agreement with the relative anisotropy of the conductivity.

The measured values are also much higher than the manufacturer-stated values in section 4.3.1. This could be due to reduced surface contact between the probes and samples, particularly in the x-direction from the ridges and valleys at each layer change. This could have been reduced with conductive paint on the surface of the cube to give greater contact area, but the porous nature of the material prohibited the use of liquids.

CHAPTER 5: HIGH CONDUCTIVITY THOUGH LIQUID GALLIUM INFILTRATION

Ideally, high conductivity in 3D printed structures would be obtained though direct printing of metal, such as copper. This element has a bulk resistivity of 1.678 x 10^{-8} Ωm[36], giving it a thin wire linear resistance of $R < 1\ \Omega/\text{m}$. This is well below the limit stated in chapter 2. Printing with copper would allow for 3D metamaterial fabrication without being limited to assemblies of 2D circuit boards[25].

The challenge of low-cost 3D printing with metal lies in the vastly different temperature regimes at which the materials can be deposited. High temperature thermoplastics for 3d printing, such as nylon, are melted and manipulated at around 250°C, while the melting point of pure copper is 1085°C. Due to the temperature difference, these two deposition processes are incompatible.

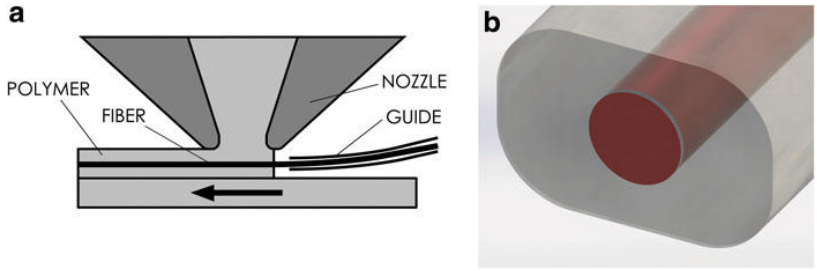

Figure 24: The FEAM method injects a continuous metal wire into the thermoplastic after extrusion[37]

5.1 Wire Printing

The spooled filament nature of FDM suggests the possibility of embedding copper wire into the printing process. The SpoolHead project attempts this by adding a wire-feed in the form of an extra extruder mounted to the print head[38]. Another venture into wire printing is the Fiber Encapsulation Additive Manufacturing (FEAM) method. This process injects a wire into the material at the site of the filament nozzle[37] (figure 24).

While there has been progress on these ambitious projects, both require heavy modification to the fabricating machine, such as the second extruder and wire cutter of the SpoolHead method, and the mobile wire guide on the FEAM printer.

5.2 Liquid Deposition

Although FDM printers predominantly heat and deposit thermoplastics, they are not restricted to these materials. Several projects have used these printers to deposit liquids and pastes through CNC syringes. One such printer is the Voxel8, an FDM machine with a second extruder for depositing a silver-based conductive ink[39]. While this could be a solution to 3D printed metamaterials, the goal is to fabricate with minimal modifications to existing low-cost machines.

The search for high conductivity at temperatures compatible with current thermoplastic filaments, and the emergence of metallic inks in 3D printers, has lead this project to use liquid gallium. The properties of this element are outlined in the next section.

Figure 25: Drop of liquid gallium slightly above room temperature

5.3 Gallium

Elemental gallium (figure 25) has a melting point $T_{m,Ga}$ of 29.8°C, slightly above room temperature, and resistivity of 13.6 x 10^{-8} Ωm[36]. In its liquid form, it has a high surface tension of approximately 500 mJ/m^2[40]. These properties are desirable in using this element in the 3D printing process, though direct printing, or as a post processing step.

Liquid gallium could be incorporated into the FDM process though a simple syringe heated above $T_{m,Ga}$. This would ensure the gallium remains in a liquid form, and could be dispensed on demand during polymer printing. However, FDM printed objects are not watertight, and can be subject to delamination issues, making this an unreliable method.

Unlike FDM, SLA printed objects are often watertight, but restricted to a single material. This restriction forces the use of gallium in the post-processing step. By printing 3D microfluidic channels with an SLA printer, liquid gallium could be in-

jected, via heated syringe, into the printed object. This was the method chosen to add a highly conductive element to a 3D printed metamaterial, using the process described in the next chapter.

CHAPTER 6: 3D PRINTED EXTENDED S-SRR

The ES-SRR, described in section 2.4, is the ideal structure for a gallium-injected metamaterial. The continuous nature of the extended S-shape would allow for the liquid metal to flow from one end of the bulk material to the other, creating several unit cells with one injection. This is preferable to the discrete SRR described in section 2.2, where each meta-atom would require an injection. This chapter describes the design and fabrication of a 3D printed ES-SRR, concluding with results and discussion of free space refractive index measurements of a single extended s-structure.

6.1 Design

6.1.1 Simulation

COMSOL Multiphysics was used to simulate the resonant response of the S-structure. To ensure proper fabrication on a Form1+ SLA printer, the minimum feature size was 1.0 mm. After optimizing the dimensions for a response between 6 and 8 GHz, the structure in figure 26 was obtained. This unit cell is to be extended as described in section 2.4.

The benefit of the ES-SRR is its ability to tune ϵ_{eff} and μ_{eff} using a single structure. This metamaterial assembly can achieve simultaneous negative values for these parameters, reaching a negative refractive index n. Simulating the structure in figure 26 revealed resonant interaction and a negative index between 6 and 8 GHz.

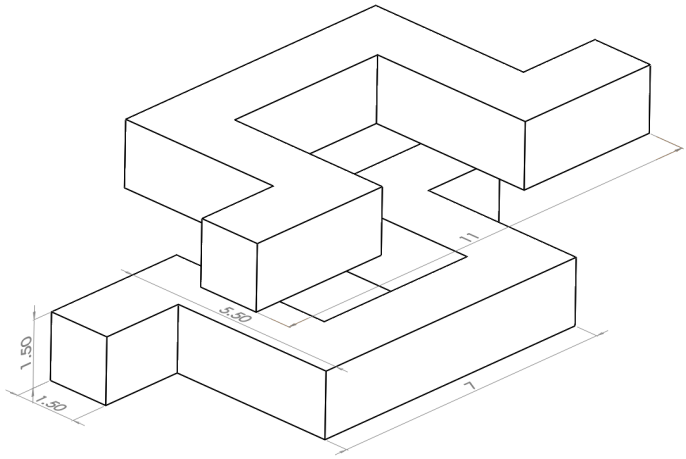

Figure 26: The unit cell of the ES-SRR. All dimensions are in millimeters

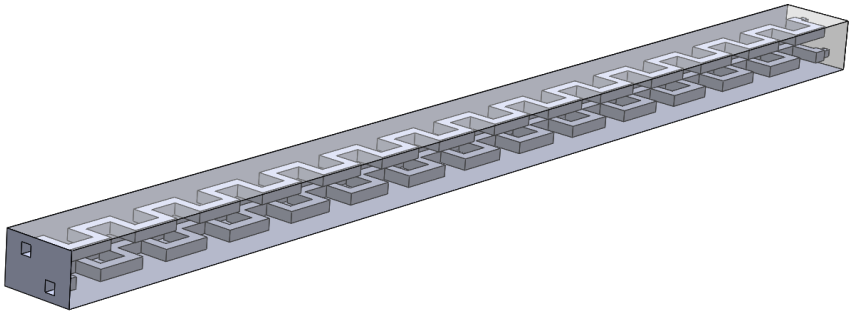

Figure 27: A single ES-SRR, designed in Solidworks. Longest dimension is 154 mm

6.1.2 CAD

Using the dimensions of the unit cell, the extended structure was designed in Solidworks. Microfluidic channels with a cross-sectional area of 1.5 x 1.5 mm^2 extended the length of the structure, with injection and relief ports on opposing ends, as seen in figure 27. Internally, the S-elements were separated by 2 mm, with 1 mm spacing on top and bottom, and 2.35 mm on the left and right. These dimensions were determined by the previous simulation work, and ensure proper spacing between meta-atoms should they be used in a bulk metamaterial assembly.

Figure 28: ES-SRR with support structures after printing

6.2 Fabrication

6.2.1 Printing

The CAD file was saved as an STL, and imported into Preform, the slicing software for the SLA printer. Layer height was set at 25 μm, and several copies of the structure were sliced for printing. Print time was approximately 30 hours, due to the high resolution and the long-edge dimension (154 mm) of the structure (figure 28).

Using the proprietary Formlabs black resin gave the highest resolution and most accurate feature dimensions. A second structure was modeled without an enclosing upper surface and printed to verify internal feature formation (figure 29).

6.2.2 Post-processing

After printing, the structures were placed in a room-temperature isopropal alcohol bath for 20 minutes to remove uncured resin. During this cleaning, a syringe was used to inject alcohol into the hollow channels to remove uncured resin and verify a

Figure 29: Cut-away view of ES-SRR to verifiy internal feature formation.

continuous path from injection to relief port. On average, approximately half of the structures had a defect that blocked one or both of the channels.

The hollow ES-SRRs were removed from the alcohol bath and allowed to dry in ambient conditions. An air-filled syringe was used to force the majority of alcohol from the interior channels.

6.2.3 Gallium Infiltration

To melt the initially solid gallium, the element was placed in a glass container on a hot-plate. Approximately 1 mL of liquid gallium was drawn into a syringe, and temperature was maintained by intermittent use of a heat gun on the syringe. The heat gun was also used to raise the temperature of the hollow ES-SRR to prevent gallium from solidifying during infiltration. From a port on one side of the structure, the liquid element was continuously injected until it flowed out the relief port. The high surface tension of gallium and horizontal orientation of the channels ensured full infiltration without loss of metal (figure 31).

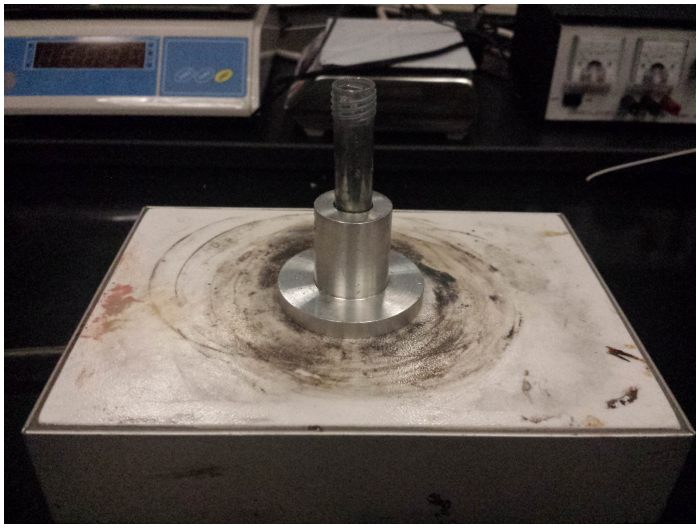

Figure 30: Liquid gallium on a hot-plate

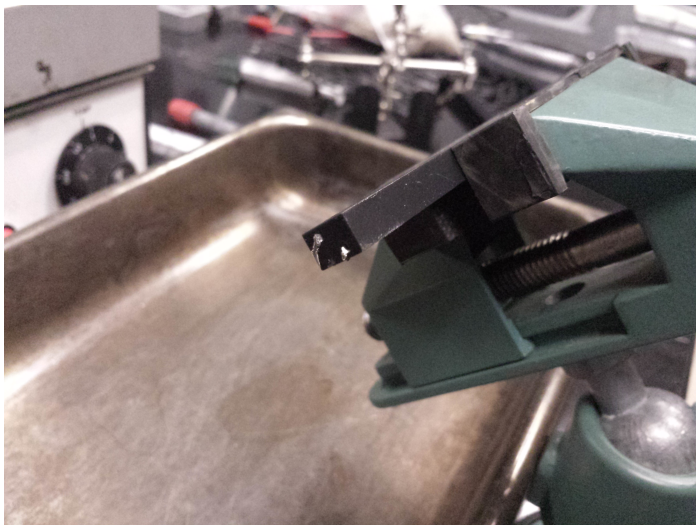

Figure 31: Gallium-infiltrated ES-SRR

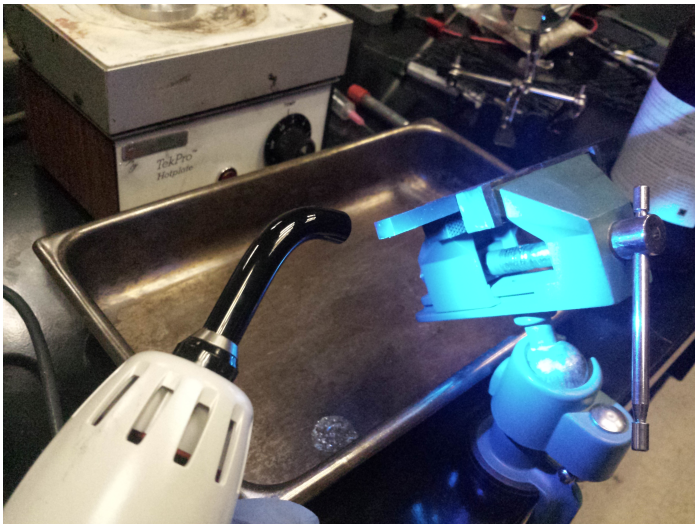

Figure 32: A UV light was used to seal the injection and relief ports

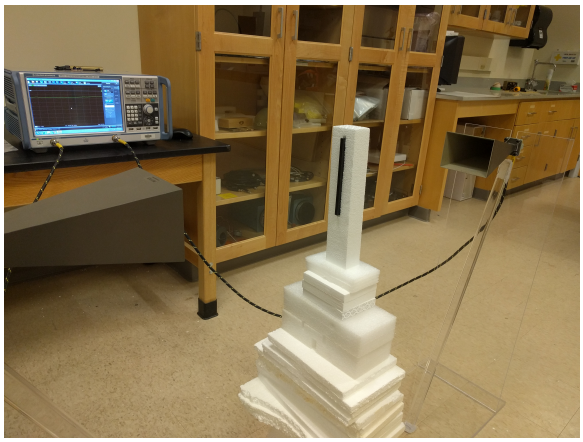

Figure 33: S-element free space measurements

The gallium was allowed to cool and solidify. Heat was applied to melt and remove gallium that expanded out of the injection and relief ports during solidification. Uncured black resin was used to cover the ports, and solidified with a UV light (figure 32).

6.3 Results

The sealed gallium-infiltrated structure was placed between two microwave horns and subjected to free space measurements between 7 and 13 GHz (figure 33). A

resonant response was apparent in the 8 to 10 GHz range.

These initial results indicate a successful resonant metamaterial fabrication using liquid gallium as the conductive element, enclosed in a 3d printed structure.

CHAPTER 7: CONCLUSIONS

7.1 Conductive Doped Polymers

The resistance tests of chapter 4 have proven that PLA doped with carbon black is not conductive enough to be applied to resonant metamaterial fabrication. Future work seeking improved conductivity would require exploration of other conductive embedded particles, such as graphene or copper. Processing of the current material could also be a pathway to lower resistance. Annealing under pressure could be a solution to the low conductivity, reforming the printed polymer structure with a more dense packing of the conductive particles.

Despite the low conductivity, this project took the first steps to characterizing the electrical properties of 3D printed objects utilizing conductive doped polymer. By understanding these properties, the material could be used in analog 3D printed sensors, detecting a change in conductivity when exposed to environmental stimuli.

7.2 Gallium-infiltrated 3D Printed Structures

With the resonant response described in section 6.3, this project proves the viability of using 3D printed structures as a host medium for conductive elements for the purpose of resonant metamaterial fabrication. Initial results were noisy and demonstrated some unaccounted loss. Current and future work includes more free space measurements on the ES-SRR structures, and a study on the solidified proprietary

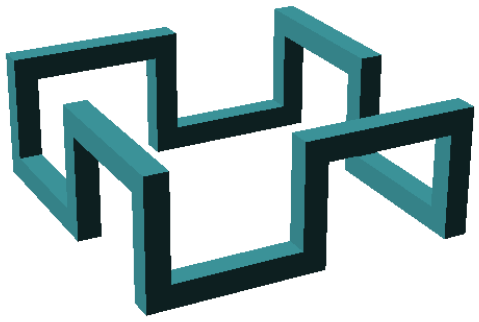

Figure 34: An example structure with full 3D geometry

printer resin to further understand its electromagnetic properties.

This project has also provided a new method of fabrication that can be applied beyond the ES-SRR in chapter 6. Structures with continuous elements extending in all 3 coordinates (see example, figure 34) can be fabricated using a 3D printer and injected with highly conductive liquid metal. Using this project as a foundation, novel theories may overcome the fabrication barrier, leading to a new generation of metamaterials.

REFERENCES

[1] Shu Zhang, Leilei Yin, and Nicholas Fang. Focusing ultrasound with an acoustic metamaterial network. *Physical Review Letters*, 102(19):1–5, 2009.

[2] J. B. Pendry, a. J. Holden, D. J. Robbins, and W. J. Stewart. Magnetism from conductors and enhanced nonlinear phenomena. *IEEE Transactions on Microwave Theory and Techniques*, 47(11):2075–2084, 1999.

[3] Viktor G Veselago. THE ELECTRODYNAMICS OF SUBSTANCES WITH SIMULTANEOUSLY NEGATIVE VALUES OF epsilon AND mu. *Soviet Physics Uspekhi*, 10(4):509–514, 1968.

[4] J B Pendry, a J Holden, D J Robbins, and W J Stewart. Low frequency plasmons in thin-wire structures. *Journal of Physics: Condensed Matter*, 10(22):4785–4809, 1999.

[5] Hongsheng Chen, Li-Xin Ran, Huang-Fu Jiang Tao, Xian-Min Zhang, Kang-Sheng Cheng, Tomasz M. Grzegorczyk, and Jin Au Kong. Magnetic Properties of S-Shaped Split-Ring Resonators. *Progress In Electromagnetics Research*, 51:231–247, 2005.

[6] R. A. Shelby, D. R. Smith, S. C. Nemat-Nasser, and S. Schultz. Microwave transmission through a two-dimensional, isotropic, left-handed metamaterial. *Applied Physics Letters*, 78(4):489–491, 2001.

[7] Anthony Grbic and George V. Eleftheriades. Overcoming the Diffraction Limit with a Planar Left-Handed Transmission-Line Lens. *Physical Review Letters*, 92(11):117403–1, 2004.

[8] Costas M. Soukoulis and Martin Wegener. Past Achievements and Future Challenges in 3D Photonic Metamaterials. pages 1–18, 2011.

[9] R A Shelby, D R Smith, and S Schultz. Experimental verification of negative index of refraction. *Science*, 292:77–79, 2001.

[10] D Schurig, J J Mock, B J Justice, S a Cummer, J B Pendry, a F Starr, and D R Smith. Metamaterial electromagnetic cloak at microwave frequencies. *Science (New York, N.Y.)*, 314(5801):977–980, 2006.

[11] M. Gokkavas, K. Guven, I. Bulu, K. Aydin, R. S. Penciu, M. Kafesaki, C. M. Soukoulis, and E. Ozbay. Experimental demonstration of a left-handed metamaterial operating at 100 GHz. *Physical Review B - Condensed Matter and Materials Physics*, 73(19):4–7, 2006.

[12] Shuang Zhang, Wenjun Fan, N C Panoiu, K J Malloy, R M Osgood, and S R J Brueck. Experimental Demonstration of Near-Infrared Negative-Index Metamaterials. *Physical Review Letters*, 95(13), 2005.

[13] Ruben Maas, James Parsons, Nader Engheta, and Albert Polman. Experimental realization of an epsilon-near-zero metamaterial at visible wavelengths. *Nature Photonics*, 7(11):907–912, 2013.

[14] John B. Pendry and Contemporary Physics. Negative refraction. *Contemporary Physics*, 45(3):191–202, 2004.

[15] Charles W. Hull. Apparatus for production of threedimensional objects by stereolithography. 1986.

[16] E. Sachs, M. Cima, and J. Cornie. Three-Dimensional Printing: Rapid Tooling and Prototypes Directly from a CAD Model. *CIRP Annals - Manufacturing Technology*, 39(1):201–204, 1990.

[17] S. Scott Crump. Apparatus and Method for Creating Three-Dimensional Objects. page 15, 1992.

[18] Kaufui V. Wong and Aldo Hernandez. A Review of Additive Manufacturing. *ISRN Mechanical Engineering*, 2012:1–10, 2012.

[19] Rhys Jones, Patrick Haufe, Edward Sells, Pejman Iravani, Vik Olliver, Chris Palmer, and Adrian Bowyer. RepRap the replicating rapid prototyper. *Robotica*, 29(January 2011):177–191, 2011.

[20] Nick Bilton. Disruptions: On the Fast Track to Routine 3-D Printing, 2013.

[21] Cesar R. Garcia, Jesus Correa, David Espalin, Jay H. Barton, Raymond C. Rumpf, Ryan Wicker, and Virgilio Gonzalez. 3D Printing of Anisotropic Metamaterials. *Progress In Electromagnetics Research Letters*, 34(July):75–82, 2012.

[22] Yaroslav Urzhumov, Nathan Landy, Tom Driscoll, Dimitri Basov, and David R Smith. Thin low-loss dielectric coatings for free-space cloaking. *Optics Letters*, 38(10):1606–8, 2013.

[23] Anthony Fox and Anthony Fox. Optical Properties of Solids (Oxford Master Series in Condensed Matter Physics), 2001.

[24] Tuck C. Choy. *Effective Medium Theory: Principles and Applications*. Oxford University Press, 2 edition, 2015.

[25] Hongsheng Chen, Lixin Ran, Jiangtao Huangfu, Xianmin Zhang, Kangsheng Chen, Tomasz M. Grzegorczyk, and Jin Au Kong. Left-handed materials composed of only S-shaped resonators. *Physical Review E - Statistical, Nonlinear, and Soft Matter Physics*, 70(5 2):1–4, 2004.

[26] Samuel H. Huang, Peng Liu, Abhiram Mokasdar, and Liang Hou. Additive manufacturing and its societal impact: A literature review. *International Journal of Advanced Manufacturing Technology*, 67(5-8):1191–1203, 2013.

[27] Gideon N. Levy, Ralf Schindel, and J.P. Kruth. Rapid Manufacturing and Rapid Tooling With Layer Manufacturing (Lm) Technologies, State of the Art and Future Perspectives. *CIRP Annals - Manufacturing Technology*, 52(2):589–609, 2003.

[28] LE Roscoe. Stereolithography interface specification [Text], 1988.

[29] Yasushi Ito and Kazuhiro Nakahashi. Surface triangulation for polygonal models based on CAD data. *International Journal for Numerical Methods in Fluids*, 39(1):75–96, 2002.

[30] Ian Gibson, D.W. David W Rosen, and Brent Stucker. *Additive Manufacturing Technologies: Rapid Prototyping to Direct Digital Manufacturing*, volume 54. 2009.

[31] Formlabs. Form1+ High-Resolution Desktop 3d Printer - Formlabs, 2016.

[32] Jason L Rhoads. Basic Explanation of Creep Processes, CA 94720-1730. pages 1–8, 2013.

[33] D Stauffer and a Aharony. Introduction to Percolation Theory. *Computer*, 1(4):192, 1994.

[34] Jan Chan Huang. Carbon black filled conducting polymers and polymer blends. *Advances in Polymer Technology*, 21(4):299–313, 2002.

[35] Simon J. Leigh, Robert J. Bradley, Christopher P. Purssell, Duncan R. Billson, and David A. Hutchins. A Simple, Low-Cost Conductive Composite Material for 3D Printing of Electronic Sensors. *PLoS ONE*, 7(11):1–6, 2012.

[36] David R. Lide. *CRC Handbook of Chemistry and Physics, 92nd Edition*, volume 53. 2011.

[37] Matt Saari, Bryan Cox, Edmond Richer, Paul S Krueger, and Adam L Cohen. Fiber Encapsulation Additive Manufacturing: An Enabling Technology for 3D Printing of Electromechanical Devices and Robotic Components. *3D Printing and Additive Manufacturing*, 2(1):32–39, 2015.

[38] Jacob Bayless, Mo Chen, and Bing Dai. Wire Embedding 3D Printer. *Physics*, 2010.

[39] Dario Borghino. Voxel8 Paves the Way for 3D-Printed Electronics. *Gizmag*, 2015.

[40] M R Khan, C B Eaker, E F Bowden, and M D Dickey. Giant and switchable surface activity of liquid metal via surface oxidation. *Proc Natl Acad Sci U S A*, 111(39):14047–14051, 2014.